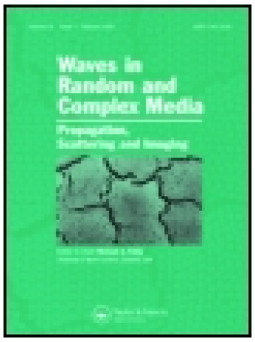

Waves in Random and Complex Media

ISSN: (Print) (Online) Journal homepage: https://www.tandfonline.com/loi/twrm20

Investigation of photonic band gap properties of one-dimensional magnetized plasma spherical photonic crystals

Tian-Qi Zhu, Jia-Tao Zhang & Hai-Feng Zhang

To cite this article: Tian-Qi Zhu, Jia-Tao Zhang & Hai-Feng Zhang (2023): Investigation of photonic band gap properties of one-dimensional magnetized plasma spherical photonic crystals, Waves in Random and Complex Media, DOI: 10.1080/17455030.2023.2172232

To link to this article: https://doi.org/10.1080/17455030.2023.2172232

Published online: 31 Jan 2023.

WAVES IN RANDOM AND COMPLEX MEDIA
https://doi.org/10.1080/17455030.2023.2172232

Investigation of photonic band gap properties of one-dimensional magnetized plasma spherical photonic crystals

Tian-Qi Zhu, Jia-Tao Zhang and Hai-Feng Zhang

College of Electronic and Optical Engineering & College of Flexible Electronics (Future Technology), Nanjing University of Posts and Telecommunications, Nanjing, People's Republic of China

ABSTRACT

Utilizing the transfer matrix method (TMM), the magnetic and electric field equations of Maxwell's system of equations in the spherical coordinate system are constructed. By combining the solution of the spherical Bessel equation to theoretically treat the magnetic and electric fields of a one-dimensional (1-D) magnetized plasma spherical photonic crystals (MPSPCs), detailed expressions for the transmission properties and dispersion relations of 1-D MPSPCs are obtained. The structure of 1-D MPSPCs is also designed, and the effects of the cyclotron frequency of plasma, incidence angle, collision frequency, plasma frequency, structure, dissipation factor and plasma thickness on the photonic band gaps (PBGs) features are discussed. With the adjustment of these parameters, the impact of the collision frequency on the transmission properties is extraordinarily insignificant. The plasma frequency and the cyclotron frequency of plasma have quite similar effects on the PBGs. The variation of incidence angle and plasma frequency thickness affects not only the position of PBGs but also the amount of them. The difference in structure and the change in dissipation factor have no effect on the distribution of PBGs and only a slight effect on the amplitude of the transmission spectra.

ARTICLE HISTORY
Received 15 August 2022
Accepted 16 January 2023

KEYWORDS
Spherical photonic crystals; magnetized plasma material; photonic band gaps; dispersion relation; transfer matrix method

1. Introduction

Since Yablonovitch [1] and John [2] proposed the concept of photonic crystals (PCs) in 1987, PCs have been the focus of research by scholars in the world. At certain frequencies, electromagnetic waves cannot propagate in PCs, forming photonic band gaps (PBGs) [3,4]. PCs use periodic dielectric structures to modulate electromagnetic waves, and the PBGs formed to offer the possibility of suppressing spontaneous radiation [5]. The discovery of PBGs has led scholars in the fields of photonics [6], electronics [7], and materials physics [8] to make PCs a focus of research, which has brought numerous new applications [9,10].

The one-dimensional (1-D) PCs are of high interest due to their easy fabrication and simple structure. The transmission properties of 1-D PCs can be investigated using the transfer matrix method (TMM). The application of 1-D PCs in the fields of metamaterials [11–13] and superconductors [14–17] have made remarkable development, and their transmittance,

CONTACT Hai-Feng Zhang hanlor@163.com

reflectance, and dispersion have been studied intensively. Meanwhile, a multitudinous variety of 1-D PCs-based sensors have been designed in combination with their transmission properties for a wide range of applications such as biosensing [18–21], temperature sensing [22], and physical quantity measurement [23,24]. There are plenty of different forms of electromagnetic waves. With continuous research, researchers have gradually shifted the focus of research from plane waves to cylindrical waves, and 1-D cylindrical photonic crystals (CPCs) have gradually become a research hotspot for scholars at home and abroad [25,26]. Similar to 1-D planar photonic crystals (PPCs), 1-D CPCs can also be processed using the TMM [27–30]. The theoretical development of 1-D CPCs has significant implications in the field of optical fibers [31] and waveguides [32]. In addition to cylindrical waves, spherical waves are also an essential form of electromagnetic waves. The superior optical properties of 1-D CPCs have led scholars to wonder whether symmetrically strong 1-D spherical photonic crystals (SPCs) have more powerful transmission properties. Laviada *et al.* simulated a new set of spherical waves and used a much smaller number of waves than the original to model the field emitted from an element [33]. In 2016, Wendel and his colleagues solved the problem of the propagation of arbitrary incident waves with the elimination of the prefactor of the radial spherical Bessel function [34]. The above research has refined the theory of spherical waves and laid the foundation for the study of 1-D SPCs. Nowadays, 1-D SPCs are widely used in biological [35], electronic communication [36], and sensor fields [37] and have tremendous research and development prospects.

The concept of 1-D magnetized plasma photonic crystals (MPPCs) was first proposed by the Japanese scholars Hojo and Mase [38]. In this study, they theoretically deduced the dispersion relation of 1-D MPPCs and performed a detailed analysis. Laxmi and Parmanand derived the calculations of the finite and infinite period structure of the plasma [39]. The properties of the PBGs are discussed in terms of plasma density, plasma width, and unit cell number. Numerical simulations of non-magnetized plasma and dielectric materials using the finite difference time domain method were carried out by Liu and his coworkers [40]. Some of the parameters in 1-D MPPCs can be changed, which makes them tunable [41,42]. This feature makes 1-D MPPCs of considerable interest for the design of space filters [43], tunable ultrawideband absorbers [44], and multichannel filters [45]. The non-reciprocal properties of 1-D plasma CPCs have been investigated by Wang *et al.* [46]. Although there are numerous studies on plasma and 1-D PCs, the system of PCs is not well established and the main research of 1-D SPCs is still at the stage of theory and design of simple devices. In 2016, Wendel and his team studied the unfolding of vector spherical waves in electromagnetic fields and obtained a complete set of radially independent amplitudes of vector spherical wave functions [47]. What's more, 1-D SPCs are momentous in optical displays [48], millimeter wave communication [49], nanomaterials [50], and other fields. It is no exaggeration to say that 1-D SPCs have well-defined geometrical properties and adapt to a wide range of physical scenarios, there is no exploration keeping a watchful eye on the combination of 1-D SPCs and plasma to construct adaptable and multi-functional 1-D magnetized plasma spherical photonic crystals (MPSPCs).

In this paper, a systematic theoretical analysis of the transmission properties of 1-D SPCs with magnetized plasma using TMM is carried out, and detailed expressions for the reflectance, transmittance, absorptance and dispersion relations are acquired. Due to the magneto-optical effect, the study is concentrated on the case of TM waves. A 1-D MPSPCs structure was also constructed, and the effects of the cyclotron frequency of plasma,

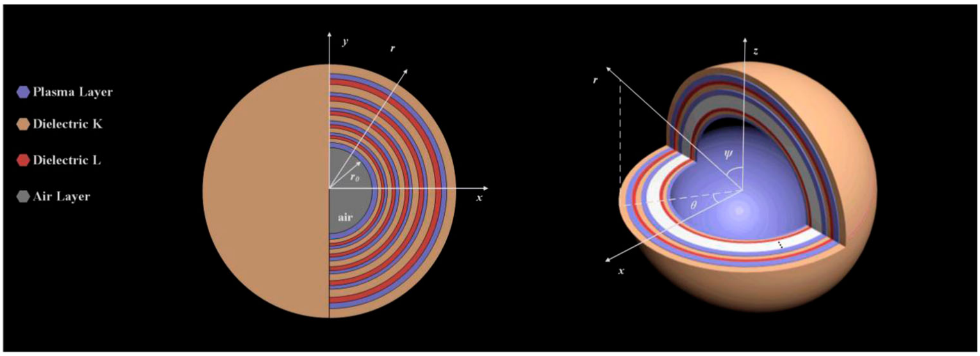

Figure 1. The structure chart of 1-D MPSPCs with periodic arrangement of the general dielectric K, the general dielectric L and the plasma.

incidence angle, collision frequency, plasma frequency, structure, dissipation factor, and plasma thickness on the PBGs performance of 1-D MPSPCs are investigated. It is revealed that 1-D MPSPCs not only have superior forbidden band properties but also have tunability and favorable absorption properties. Their superior transmission properties provide new insights into the design of tunable electromagnetic devices and reflectors. It is worth mentioning that this paper only focuses on the theoretical investigation, and how to realize and verify the given 1-D MPSPCs or obtained results in the experiment is beyond scope of this paper.

2. Simulation model and formulation

The structure of 1-D MPSPCs is shown in Figure 1, which consists of the general dielectric K, the general dielectric L and the plasma P arranged periodically according to the $(\mathrm{PKL})^N$ form, where N represents the number of periods. Normalize d with $d = 1$, initial radius r_0 is taken as $20d$, thickness d_A of general dielectric K is $0.2d$, thickness d_B of general dielectric L is $0.35d$, and thickness d_P of plasma P is $0.45d$. The effective refractive index of the general dielectric K is $n_K = 2.8$, the effective refractive index of the general dielectric L is $n_L = 2.1$, and the effective magnetic permeability of plasma P will be described in detail below.

Due to the special geometric properties of the sphere, inspired by the idea of the micro-element method and the definition of the incidence angle under the cylindrical photonic crystal [27], the TE waves and TM waves are defined by taking the profile of the spherical wave and 1-D MPSPCs parallel to the wave propagation direction, as shown in Figure 2. For this plane, the electric field $\boldsymbol{E}$ is perpendicular to the plane, the magnetic field $\boldsymbol{H}$ is parallel to the plane, and the wave vector $\boldsymbol{k}$ indicates the propagation direction. Therefore, the electric field $\boldsymbol{E}$ takes the form of $\boldsymbol{E} = (0, E_\theta, 0)$ in the TE waves and the magnetic field $\boldsymbol{H}$ takes the form of $\boldsymbol{H} = (H_r, 0, H_\varphi)$. By analogy, in the TM waves, the electric field E is denoted as $\boldsymbol{E} = (E_r, 0, E_\varphi)$ and the magnetic field H is denoted as $\boldsymbol{H} = (0, H_\theta, 0)$. 1-D MPSPCs and the spherical waves demonstrably have an intersection point. From the intersection point, the tangents to 1-D MPSPCs and the spherical waves are made respectively, and the angle between the two tangents is the angle of incidence, as shown in Figure 2. The electromagnetic wave propagates from the yoz plane at an angle of incidence α. It is prescribed that

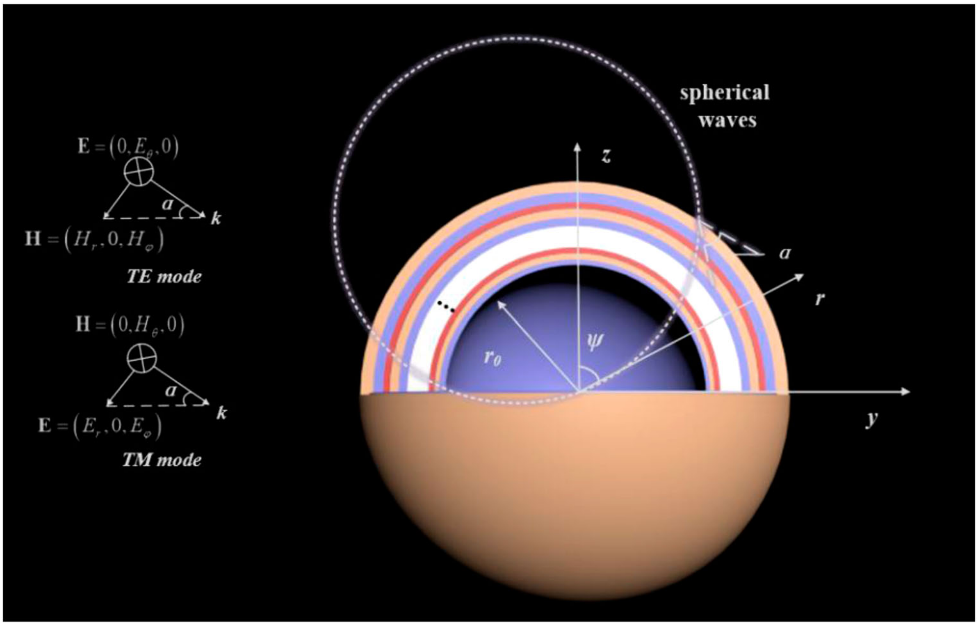

Figure 2. The main image of 1-D MPSPCs showing in detail the angle of incidence α, electromagnetic direction and magnetic field direction.

under the TE polarization the wave vector ***k*** is always perpendicular to the magnetic field ***H***. Equally, under TM polarization the electric field ***E*** invariably remains perpendicular to the wave vector ***k***.

The system of Maxwell's equations with time using plasma is expressed as:

$$\nabla \times \boldsymbol{E} = -\mu_0 \frac{\partial \boldsymbol{H}}{\partial t} \tag{1}$$

$$\nabla \times \boldsymbol{H} = \varepsilon_0 \frac{\partial \boldsymbol{E}}{\partial t} + \boldsymbol{J} \tag{2}$$

$$\frac{d\boldsymbol{J}}{dt} + v_c \boldsymbol{J} = \varepsilon_0 \omega_p^2 \mathbf{E} + \boldsymbol{\omega_c} \times \boldsymbol{J} \tag{3}$$

where ***J*** is a vector quantity, called polarization current density, which can be decomposed along the three directions r, θ, and ψ. v_c is the collision frequency and ω_p is the plasma frequency. ω_c is the cyclotron frequency of plasma, denoted as $eB_0/m\boldsymbol{e_\theta}$. In the initial state, define normalized frequency $\omega_0 = 2\pi c/d$, $\omega_p = \omega_0$, $v_c = 0.0001\omega_p$, and $\omega_c = 0$.

Decomposing Equation (3) in the three directions of r, θ, and ψ, the following is obtained.

$$(-i\omega + v_c)J_r = \varepsilon_0 \omega_p^2 E_r + \omega_c J_\varphi \tag{4}$$

$$(-i\omega + v_c)J_\theta = \varepsilon_0 \omega_p^2 E_\theta \tag{5}$$

$$(-i\omega + v_c)J_\varphi = \varepsilon_0 \omega_p^2 E_\varphi - \omega_c J_r \tag{6}$$

In consideration of the relationship between $\boldsymbol{J}$ and $\boldsymbol{E}$, $\boldsymbol{J}$ is expressed in the following form:

$$\begin{pmatrix} J_r \\ J_\theta \\ J_\varphi \end{pmatrix} = \varepsilon_0 \begin{pmatrix} \dfrac{i\omega_p^2(\omega + i v_c)}{(\omega + i v_c)^2 - \omega_c^2} & 0 & -\dfrac{\omega_p^2 \omega_c}{(\omega + i v_c)^2 - \omega_c^2} \\ 0 & \dfrac{i\omega_p^2}{\omega + i v_c} & 0 \\ \dfrac{\omega_p^2 \omega_c}{(\omega + i v_c)^2 - \omega_c^2} & 0 & \dfrac{i\omega_p^2(\omega + i v_c)}{(\omega + i v_c)^2 - \omega_c^2} \end{pmatrix} \begin{pmatrix} E_r \\ E_\theta \\ E_\varphi \end{pmatrix} \tag{7}$$

Since Equation (7) gives the relationship between $\boldsymbol{J}$ and $\boldsymbol{E}$, Equation (2) can be rewritten as:

$$\nabla \times \boldsymbol{H} = \varepsilon_0 \varepsilon_p \frac{\partial \boldsymbol{E}}{\partial t} \tag{8}$$

where

$$\boldsymbol{\varepsilon_p} = \begin{pmatrix} \varepsilon_1 & 0 & i\varepsilon_2 \\ 0 & \varepsilon_3 & 0 \\ -i\varepsilon_2 & 0 & \varepsilon_1 \end{pmatrix} \tag{9}$$

$$\varepsilon_1 = 1 - \frac{\omega_p^2(\omega + i v_c)}{\omega[(\omega + i v_c)^2 - \omega_c^2]} \tag{10}$$

$$\varepsilon_2 = -\frac{\omega_p^2 \omega_c}{\omega[(\omega + i v_c)^2 - \omega_c^2]} \tag{11}$$

$$\varepsilon_3 = 1 - \frac{\omega_p^2}{\omega(\omega + i v_c)} \tag{12}$$

Under the TM polarization, the electric and magnetic fields are represented as:

$$\boldsymbol{E} = e^{-i\omega t}(E_r, 0, E_\varphi) \tag{13}$$

$$\boldsymbol{H} = e^{-i\omega t}(0, H_\theta, 0) \tag{14}$$

Maxwell's system of equations is formulated as follows:

$$\frac{1}{r\sin\theta}\left[\frac{\partial E_r}{\partial \varphi} - \frac{\partial}{\partial r}(r\sin\theta E_\varphi)\right] = -i\omega\mu_0 H_\theta \tag{15}$$

$$\frac{1}{r^2\sin\theta}\left[\frac{\partial}{\partial \theta}(r\sin\theta H_\varphi) - \frac{\partial}{\partial \varphi}(r H_\theta)\right] = i\omega\varepsilon_0(\varepsilon_1 E_r + i\varepsilon_2 E_\varphi) \tag{16}$$

$$\frac{1}{r}\left[\frac{\partial}{\partial r}(r H_\theta) - \frac{\partial H_r}{\partial \theta}\right] = i\omega\varepsilon_0(-i\varepsilon_2 E_r + \varepsilon_1 E_\varphi) \tag{17}$$

Combined with the transmission properties of spherical waves, the derivative of ψ can be omitted.

$$\frac{1}{r^2\sin\theta}\left[-\frac{\partial}{\partial \varphi}(r H_\theta)\right] = i\omega\varepsilon_0(\varepsilon_1 E_r + i\varepsilon_2 E_\varphi) \tag{18}$$

$$\frac{1}{r}\left[\frac{\partial}{\partial r}(r H_\theta)\right] = i\omega\varepsilon_0(-i\varepsilon_2 E_r + \varepsilon_1 E_\varphi) \tag{19}$$

Simplifying Equations (18) and (19) yields:

$$E_\varphi = \frac{1}{r\omega\varepsilon_0}\frac{1}{\varepsilon_2^2-\varepsilon_1^2}\left[\frac{\varepsilon_2}{r\sin\theta}\frac{\partial(rH_\theta)}{\partial\varphi}+i\varepsilon_1\frac{\partial(rH_\theta)}{\partial r}\right] \tag{20}$$

$$E_r = \frac{1}{r\omega\varepsilon_0}\frac{1}{\varepsilon_2^2-\varepsilon_1^2}\left[\varepsilon_2\frac{\partial(rH_\theta)}{\partial r}-\frac{i\varepsilon_1}{r\sin\theta}\frac{\partial(rH_\theta)}{\partial\varphi}\right] \tag{21}$$

Substitute Equations (20) and (21) into Equation (15).

$$\frac{1}{r^2}\frac{\partial}{\partial r}\left(r^2\frac{\partial H_\theta}{\partial r}\right)+\frac{1}{r^2\sin^2\theta}\frac{\partial^2 H_\theta}{\partial\varphi^2}+k^2H_\theta=0 \tag{22}$$

Furthermore, here $k=\omega\cos\alpha\sqrt{\mu_0\varepsilon_0\varepsilon_{TM}}$, $\varepsilon_{TM}=(\varepsilon_1^2-\varepsilon_2^2)/\varepsilon_1$ and α is the incident angle. In the following, define $H_\theta(x)=V(x)\Psi(\varphi)$, where $x=kr$. Readily know the angular part of H_θ satisfies the following equation.

$$\frac{d^2\Psi}{d\varphi^2}+m^2\varphi=0 \tag{23}$$

Solving differential Equation (23) yields $\Psi\sim e^{im\varphi}$, where m is a positive integer, a negative integer, and zero.

Then let,

$$m^2=l(l+1)\sin^2\theta \tag{24}$$

Utilizing the separation of variables method, the equations on $V(x)$ are derived by combining Equations (22)–(24).

$$x^2\frac{d^2V}{dx^2}+x\frac{dV}{dx}+\left[x^2-\left(l+\frac{1}{2}\right)^2\right]V(x)=0 \tag{25}$$

It is effortless to conclude that $V(x)$ fulfills the form of the standard semi-odd order spherical Bessel equation. Therefore, $V(x)$ can be written in the form of a linear combination of spherical Bessel functions.

$$V(x)=Aj_l(x)+Bn_l(x) \tag{26}$$

Both $j_l(x)$ and $n_l(x)$ are solutions of the spherical Bessel equation of semi-odd order, and the expressions are shown below.

$$j_l(x)=\sqrt{\frac{\pi}{2x}}J_{l+\frac{1}{2}}(x)$$

$$n_l(x)=\sqrt{\frac{\pi}{2x}}N_{l+\frac{1}{2}}(x) \tag{27}$$

For simplicity, $U(x)$ is expressed as:

$$U(x)=\frac{1}{i\omega\varepsilon r}\frac{\partial}{\partial x}(xH_\theta)=\frac{1}{i\omega\varepsilon r}\left(H_\theta+x\frac{\partial H_\theta}{\partial x}\right) \tag{28}$$

Substitute Equation (26) into Equation (28)

$$U(x) = \frac{1}{i\omega\varepsilon r}[Aj_l(x) + Bn_l(x) + xAj_l{}'(x) + xBn_l{}'(x)] \tag{29}$$

Meanwhile, $j_l{}'(x)$ and $n_l{}'(x)$ are the first order derivatives of the Bessel functions, and the corresponding equations are indicated as:

$$\begin{aligned} j_l{}'(x) &= \sqrt{\frac{\pi}{2x}}J'_{l+\frac{1}{2}}(x) - \frac{1}{2}\sqrt{\frac{\pi}{2}}x^{-\frac{3}{2}}J_{l+\frac{1}{2}}(x) \\ n_l{}'(x) &= \sqrt{\frac{\pi}{2x}}N'_{l+\frac{1}{2}}(x) - \frac{1}{2}\sqrt{\frac{\pi}{2}}x^{-\frac{3}{2}}N_{l+\frac{1}{2}}(x) \end{aligned} \tag{30}$$

1-D MPSPCs are formed by periodic arrangements of plasma and general dielectrics. To obtain the transmission properties of electromagnetic waves in the multilayer dielectrics, the vector $\begin{pmatrix} V(x) \\ U(x) \end{pmatrix}$ is stipulated and the TMM is adopted to relate the homologous vectors at different radiuses.

$$\begin{pmatrix} V(x) \\ U(x) \end{pmatrix} = \mathbf{M}\begin{pmatrix} V(x_0) \\ U(x_0) \end{pmatrix} = \begin{pmatrix} M_{11} & M_{12} \\ M_{21} & M_{22} \end{pmatrix}\begin{pmatrix} V(x_0) \\ U(x_0) \end{pmatrix} \tag{31}$$

The electric and magnetic fields at r_0 and r are facile to receive the respective magnitudes, and the work to be performed now is the solution of the elements of the transmission matrix. To make the calculation easier, the method of taking special values is employed. In the first place, let,

$$\begin{aligned} V(x_0) &= 1 \\ U(x_0) &= 0 \end{aligned} \tag{32}$$

From the above derivations, we have:

$$M_{11} = V(x) = Aj_l(x) + Bn_l(x) \tag{33}$$

$$M_{21} = U(x) = \frac{1}{i\omega\varepsilon r}[Aj_l(x) + Bn_l(x) + xAj_l{}'(x) + xBn_l{}'(x)] \tag{34}$$

Assign values to $V(x)$ and $U(x)$

$$\begin{aligned} V(x_0) &= Aj_l(x_0) + Bn_l(x_0) = 1 \\ U(x_0) &= Aj_l(x_0) + Bn_l(x_0) + x_0Aj_l{}'(x_0) + x_0Bn_l{}'(x_0) = 0 \end{aligned} \tag{35}$$

Make use of Equation (35), the expressions for A and B can be determined.

$$\begin{aligned} A &= \frac{1}{j_l(x_0)n'_l(x_0) - n_l(x_0)j_l{}'(x_0)}\left[n_l{}'(x_0) + \frac{n_l(x_0)}{x_0}\right] \\ B &= \frac{1}{n_l(x_0)j_l{}'(x_0) - n'_l(x_0)j_l(x_0)}\left[j_l{}'(x_0) + \frac{j_l(x_0)}{x_0}\right] \end{aligned} \tag{36}$$

where *A* and *B* are crucial components of the elementary expressions of the matrix. Combining Equations (33), (34) and (36), the expressions for M_{11} and M_{21} are derived.

$$M_{11} = \frac{j_l(x)}{j_l(x_0)n'_l(x_0) - n_l(x_0)j_l'(x_0)}\left[n_l'(x_0) + \frac{n_l(x_0)}{x_0}\right] + \frac{n_l(x)}{n_l(x_0)j_l'(x_0) - n'_l(x_0)j_l(x_0)}\left[j_l'(x_0) + \frac{j_l(x_0)}{x_0}\right] \tag{37}$$

$$M_{21} = \frac{1}{i\omega\varepsilon r}\left\{\frac{j_l(x)}{j_l(x_0)n'_l(x_0) - n_l(x_0)j_l'(x_0)}\left[n_l'(x_0) + \frac{n_l(x_0)}{x_0}\right] + \frac{n_l(x)}{n_l(x_0)j_l'(x_0) - n'_l(x_0)j_l(x_0)}\left[j_l'(x_0) + \frac{j_l(x_0)}{x_0}\right] + \frac{xj_l'(x)}{j_l(x_0)n'_l(x_0) - n_l(x_0)j_l'(x_0)}\left[n_l'(x_0) + \frac{n_l(x_0)}{x_0}\right] + \frac{xn_l'(x)}{n_l(x_0)j_l'(x_0) - n'_l(x_0)j_l(x_0)}\left[j_l'(x_0) + \frac{j_l(x_0)}{x_0}\right]\right\} \tag{38}$$

Similarly, assigning values to $V(x)$ and $U(x)$,

$$V(x_0) = 0$$
$$U(x_0) = 1 \tag{39}$$

With Equation (31), it is possible to observe that

$$M_{12} = V(x) = Cj_l(x) + Dn_l(x) \tag{40}$$

$$M_{22} = U(x) = \frac{1}{i\omega\varepsilon r}[Cj_l(x) + Dn_l(x) + xCj_l'(x) + xDn_l'(x)] \tag{41}$$

Then we get:

$$V(x_0) = Cj_l(x_0) + Dn_l(x_0) = 0$$
$$U(x_0) = \frac{1}{i\omega\varepsilon r_0}[Cj_l(x_0) + Dn_l(x_0) + x_0Cj_l'(x_0) + x_0Dn_l'(x_0)] = 1 \tag{42}$$

Integrating Equation (42), the expressions for C and D are shown below.

$$C = \frac{1}{n_l(x_0)j_l'(x_0) - n'_l(x_0)j_l(x_0)}\left[\frac{i\omega\varepsilon}{k}n_l(x_0)\right]$$
$$D = \frac{1}{j_l(x_0)n'_l(x_0) - n_l(x_0)j_l'(x_0)}\left[\frac{i\omega\varepsilon}{k}j_l(x_0)\right] \tag{43}$$

M_{12} and M_{22} are further written as:

$$M_{12} = \frac{j_l(x)}{n_l(x_0)j_l'(x_0) - n'_l(x_0)j_l(x_0)}\left[\frac{i\omega\varepsilon}{k}n_l(x_0)\right] + \frac{n_l(x)}{j_l(x_0)n'_l(x_0) - n_l(x_0)j_l'(x_0)}\left[\frac{i\omega\varepsilon}{k}j_l(x_0)\right] \tag{44}$$

$$M_{22} = \frac{1}{i\omega\varepsilon r}\{\frac{j_l(x)}{n_l(x_0)j_l{}'(x_0) - n'_l(x_0)j_l(x_0)}\left[\frac{i\omega\varepsilon}{k}n_l(x_0)\right] + \frac{n_l(x)}{j_l(x_0)n'_l(x_0) - n_l(x_0)j_l{}'(x_0)}\left[\frac{i\omega\varepsilon}{k}j_l(x_0)\right] + \frac{xj_l{}'(x)}{n_l(x_0)j_l{}'(x_0) - n'_l(x_0)j_l(x_0)}\left[\frac{i\omega\varepsilon}{k}n_l(x_0)\right] + \frac{xn_l{}'(x)}{j_l(x_0)n'_l(x_0) - n_l(x_0)j_l{}'(x_0)}\left[\frac{i\omega\varepsilon}{k}j_l(x_0)\right]\} \quad (45)$$

At this point, the transmission matrix is derived. For wave propagation, the field can be signified as a sum of two waves in opposite directions, which can be considered as a superposition of incoming and outgoing waves. These two waves are usually represented by two Hankel functions:

$$h_1^{(1)}(x) = j_l(x) + in_l(x)$$
$$h_1^{(2)}(x) = j_l(x) - in_l(x) \quad (46)$$

The magnetic and electric fields can be expressed separately as:

$$H_\theta^+(x) = Qh_l^{(2)}(x)e^{im\varphi}$$
$$H_\theta^-(x) = Ph_l^{(1)}(x)e^{im\varphi} \quad (47)$$

$$E_\varphi^+(x) = \frac{Q}{i\omega\varepsilon r}[h_l^{(2)}(x) + xh_l^{(2)'}(x)]e^{im\varphi}$$
$$E_\varphi^-(x) = \frac{P}{i\omega\varepsilon r}[h_l^{(1)}(x) + xh_l^{(1)'}(x)]e^{im\varphi} \quad (48)$$

From Maxwell's system of equations, the following relationship between the electric field and the magnetic field can be realized.

$$C_l^{(2)}(x) = 1 + x\frac{h_l^{(2)'}(x)}{h_l^{(2)}(x)}$$
$$C_l^{(1)}(x) = 1 + x\frac{h_l^{(1)'}(x)}{h_l^{(1)}(x)} \quad (49)$$

The output waves are incident to the $r = r_0$ interface and finally exit from the $r = r_f$ interface. With the boundary conditions in mind, TMM is selected to string together 1-D SPCs at different radii. For the sake of observation and understanding, here we assume the case where the incidence angle is 0 as an example. The incident spherical wave is defined as 1 and is analogous to the Airy formula in the plane. The outgoing spherical waves can be expressed by the transmission coefficient t_d and the reflected spherical waves by the reflection coefficient r_d. The expressions for the electric and magnetic fields on both sides of the dielectric can be with a wet finger obtained by theoretical calculations using TMM, which in turn leads to the expressions for the transmission properties of 1-D MPSPCs [27] (Figure 3).

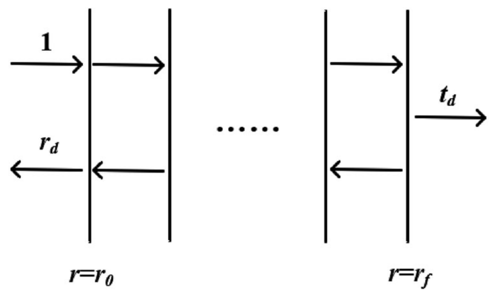

Figure 3. The schematic diagram of spherical waves propagation at positive incidence, where the surface interface is intentionally drawn as a straight line for ease of illustration.

In 1-D MPSPCs, the evanescent spherical waves are incident at r_0 and exit at r_f. The reflection coefficient r_d and transmission coefficient t_d can be described by the elements in the transmission matrix **M**.

$$\begin{pmatrix} 1+r_d \\ \frac{C_l^{(2)}(x_0)}{i\omega\varepsilon_0 r_0} + \frac{C_l^{(1)}(x_0)}{i\omega\varepsilon_0 r_0} r_d \end{pmatrix} = \boldsymbol{M}^{-1} \begin{pmatrix} t_d \\ \frac{C_l^{(2)}(x_f)}{i\omega\varepsilon_f r_f} t_d \end{pmatrix} \tag{50}$$

where,

$$\boldsymbol{M} = \boldsymbol{M_1 M_2 M_1} \cdots \boldsymbol{M_1 M_2}$$
$$\boldsymbol{M}^{-1} = \begin{pmatrix} M'_{11} & M'_{12} \\ M'_{21} & M'_{22} \end{pmatrix} \tag{51}$$

Substituting Equations (37), (38), (44) and (45) into Equation (50), the reflection coefficient r_d and transmission coefficient t_d can be expressed in terms of the elements in the transfer matrix **M**. The specific expression is written as:

$$t_d = \frac{C_l^{(1)}(x_0) - C_l^{(2)}(x_0)}{i\omega\varepsilon_0 r_0 \left[M_{11} \frac{C_l^{(1)}(x_0)}{i\omega\varepsilon_0 r_0} - M_{21} + \frac{C_l^{(2)}(x_f)}{i\omega\varepsilon_f r_f} \cdot \frac{C_l^{(1)}(x_0)}{i\omega\varepsilon_0 r_0} M_{12} - M_{22} \frac{C_l^{(2)}(x_f)}{i\omega\varepsilon_f r_f} \right]} \tag{52}$$

$$r_d = M_{11} + M_{12} \frac{C_l^{(2)}(x_f)}{i\omega\varepsilon_f r_f} \tag{53}$$

Ultimately get,

$$T = |t_d|^2 R = |r_d|^2 \tag{54}$$
$$A = 1 - T - R \tag{55}$$

Integrating the above theoretical treatment, the transmittance and reflectance formulas for 1-D MPSPCs are deduced completely.

For the periodic structure in Figure 1, the following equation can be obtained by combining Bloch's theorem.

$$\begin{pmatrix} E_{N+3} \\ H_{N+3} \end{pmatrix} = e^{ikd} \begin{pmatrix} E_N \\ H_N \end{pmatrix} \tag{56}$$

Similarly, from the TMM, the electric and magnetic fields of the N layer are related to the electric and magnetic fields of the $N + 3$ layer as follows:

$$\begin{pmatrix} E_N \\ H_N \end{pmatrix} = \boldsymbol{M_1 M_p M_2} \begin{pmatrix} E_{N+3} \\ H_{N+3} \end{pmatrix} \tag{57}$$

Combined with the knowledge associated with Bloch's theorem, we are informed that when the transmission mode and frequency are known, the difference between the fields in two cross sections at a distance of one spatial cycle length is a complex constant, and the relationship between the electric and magnetic field distribution under multiple periods can be obtained by investigating the electromagnetic properties in one period. TMM is also exploited to achieve the target of analyzing the electromagnetic wave distribution on both sides of the dielectric. By and large, use Bloch's theorem, as in Equation (56), to simplify the study range from multi-period to single-period, and employ TMM to perform the theoretical analysis, as in Equation (57), which fully takes into account the propagation of electromagnetic waves in different dielectrics, in accordance with the actual scenario.

Synthesizing Equations (55) and (56), the dispersion relation satisfies:

$$\det(\boldsymbol{M_1 M_p M_2} - e^{-ikd}) = 0 \tag{58}$$

Let,

$$\boldsymbol{M_1 M_p M_2} = \boldsymbol{M_k} = \begin{pmatrix} M_{k11} & M_{k12} \\ M_{k21} & M_{k22} \end{pmatrix} \tag{59}$$

The ultimate dispersion relationship satisfies the following equation.

$$\cos(kd) = \frac{M_{k11} + M_{k22}}{1 + \det \boldsymbol{M}_k} = \frac{M_{k11} + M_{k22}}{2} \tag{60}$$

3. Discussion

Figure 4 illustrates the reflectance spectra of ω_c changing from 0 to 1. The initial parameters are set as follows: $r_0 = 20d$, $d_A = 0.2d$, $d_B = 0.35d$, $d_P = 0.45d$, $\omega_p = \omega_0$, $v_c = 0.0001\omega_p$, and $\alpha = 0$. And we can plainly observe that a new PBG is generated between $2.3\omega_0$ and $2.5\omega_0$ as ω_c increases. Since the low reflectivity region accounts for a diminutive percentage, the following reflectance spectra and dispersion curves of specific ω_c are combined to analyze the transformation law. For the sake of representing PBGs more visually, it is decided to symbolize the location of PBGs with gray shading regions.

From Figures 5 and 6, it can become conscious that when $\omega_c = 0$, apparent PBGs can be observed at $\omega/\omega_0 = 2.02$, 2.60, and 2.87. At this stage, the external magnetic field is not available and the magneto-optical Voigt effect is not manifested in the plasma layer. If ω_c is $0.8\omega_p$, the position of PBG originally located at $\omega/\omega_0 = 2.02$ does not move significantly, but

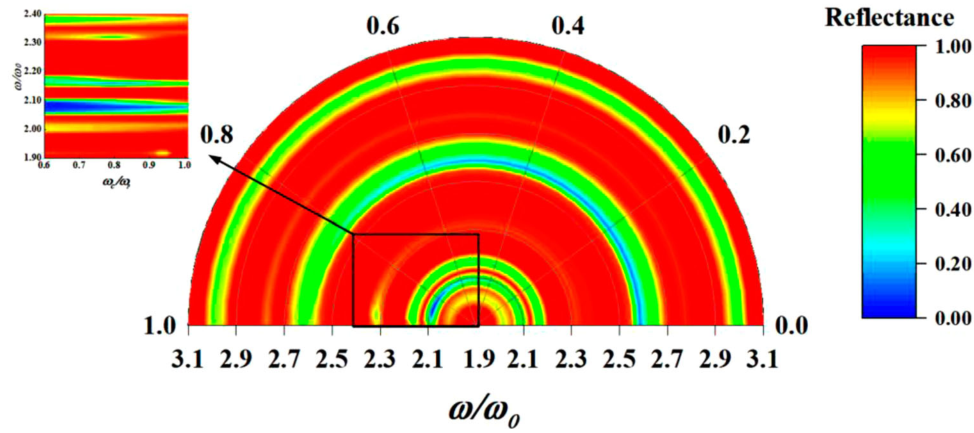

Figure 4. The reflection mapping in the case of ω_c variation, and the angle coordinate is ω_c/ω_p with $r_0 = 20d$, $d_A = 0.2d$, $d_B = 0.35d$, $d_P = 0.45d$, $\omega_p = \omega_0$, $v_c = 0.0001\omega_p$, and $\alpha = 0$.

the bandwidth rises from $0.12\omega_0$ to $0.14\omega_0$. Homoplastically, the frequency range of the PBG initially located at $\omega/\omega_0 = 2.87$ is expanded from 2.87–2.94ω/ω_0 to 2.87–2.96ω/ω_0. Compared with the PBG located at $2.60\omega_0$ at $\omega_c = 0$, the frequency coverage area of the PBG in the case of $\omega_c = 0.8$ is lessened. Further enhancing ω_c to ω_p, it can be noted that the first PBG moves from $2.02\omega_0$ to $2.04\omega_0$, showing a holistic trend toward the high-frequency region. And the bandwidths of the PBGs in this condition acquire elevated and the maximum value enlarges to $0.16\omega_0$. On the side, it is evident from the dispersion curve that when $\omega_c = 0.8\omega_p$, a PBG emerges at $\omega/\omega_0 = 2.32$, which does not appear at $\omega_c = 0$. And as ω_c ulteriorly increases to ω_p, this PBG moves to high frequencies, accompanied by an expansion in bandwidth. Combining the above analysis, it can be concluded that for the PBGs with large bandwidth, the alteration of ω_c provides a fire-new idea for the adjustment of the position and frequency range. For the PBGs having narrow bandwidths, the effect of ω_c on them is dubious, which presumably gives rise to the expansion of the forbidden bands and the shift of the PBGs positions.

Figures 7–9 are utilized below to explore the impact of α variation on the reflection spectra. Define initial parameters $r_0 = 20d$, $d_A = 0.2d$, $d_B = 0.35d$, $d_P = 0.45d$, $\omega_p = \omega_0$, and $v_c = 0.0001\omega_p$. It can be undemanding concluded from Figure 8 that the bandwidths of PBGs tend to enlarge and the number decreases as α grows. This property is extremely similar to that of 1-D PPCs, and it follows that the large incidence angles are one of the necessary conditions for the formation of the wide PBGs. The next part provides a particular analysis of α.

According to Figure 8(b), it can be figured out that the PBGs can be observed with a wet finger at $\omega/\omega_0 = 1.97$, 2.29, and 2.97 for $\alpha = 30°$. The electromagnetic waves are unable to pass through the frequency range of $1.97\omega_0$–$2.11\omega_0$, $2.29\omega_0$–$2.46\omega_0$, and $2.97\omega_0$–$3.05\omega_0$, compared to Figure 7(a), the most prominent difference is the location of the PBGs. For Figure 7(c), if $\alpha = 45°$, the PBGs are located at $2.02\omega_0$, $2.39\omega_0$, and $2.80\omega_0$ and are equipped with wide bandwidths. All the forbidden bandwidths are more than $0.1\omega_0$, and the maximum frequency region reaches $0.18\omega_0$. In the case of $\alpha = 60°$, only one PBG appears because of the large angle of incidence at this point. This PBG lies in $\omega/\omega_0 = 2.78$–3.02 and

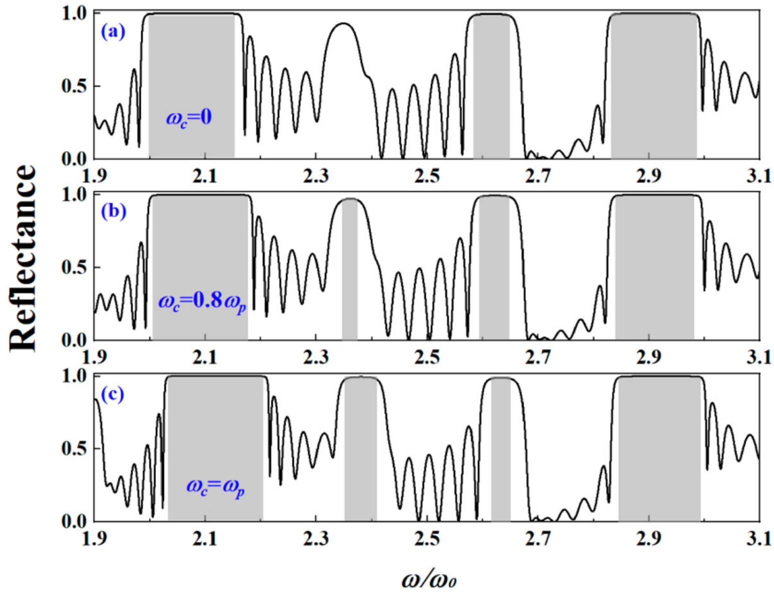

Figure 5. The influences of ω_c on the reflection spectra in case of $r_0 = 20d$, $d_A = 0.2d$, $d_B = 0.35d$, $d_P = 0.45d$, $\omega_p = \omega_0$, $v_c = 0.0001\omega_p$, and $\alpha = 0$, (a) $\omega_c = 0$, (b) $\omega_c = 0.8\omega_p$, and (c) $\omega_c = 1.2\omega_p$.

the forbidden frequency interval is much larger than the conditions of Figure 8(a–c). Meanwhile, comparing the results in Figure 8 with Figure 9, it is detected that the positions and bandwidths of the PBGs match perfectly, further proving the correctness of the derived formulas for the transmission properties of 1-D MPSPCs. In general, the large incidence angles are decisive for the formation of ultra-wide PBGs but have the disadvantage of a reduction in the number of PBGs.

The variation of the reflection spectra of v_c transformed from $0.1v_0$ ($v_c = 0.00001\omega_p$) to $10v_0$ ($v_c = 0.001\omega_p$) is offered in Figure 10. The initial parameters are stipulated as follows: $r_0 = 20d$, $d_A = 0.2d$, $d_B = 0.35d$, $d_P = 0.45d$, $\omega_p = \omega_0$, $\omega_c = 0$, and $\alpha = 0$. It can be roughly inferred from the figure that the change in v_c has an extraordinarily slight effect on the reflectance. To further investigate the effects of v_c on 1-D MPSPCs, $v_c = 0.0001\omega_p$ (in Figures 11(a) and 12(a)), $v_c = 0.00001\omega_p$ (in Figures 11(b) and 12(b)) and $v_c = 0.001\omega_p$ (in Figures 11(c) and 12(c)) are taken to compare the difference of reflectance spectra and dispersion curves among the three.

Combining Figures 11 and 12, it can be concluded that the PBGs arise at $\omega/\omega_0 = 2.02$, 2.60, and 2.87, and the transformation of v_c has almost no effect on the positions. However, the data comparison reveals that the increase of v_c has a trivial effect on the amplitude of the non-banned region. It is primarily shown that the larger the v_c is, the mild amplification of reflectance at a specific frequency in the non-banned region is observed. It makes sense to notice this property is thoroughly similar to that of 1-D PPC, which also indicates that it is unrealistic to try to obtain the change in positions and bandwidths of PBGs by adjusting v_c. Equally, the reflection spectra coincide well with the dispersion relation curves.

However, since the 1-D SPCs are analogous to the 1-D PPCs, differing only in geometric configuration and incident waveform, the superiority of the 1-D SPCs can be visualized

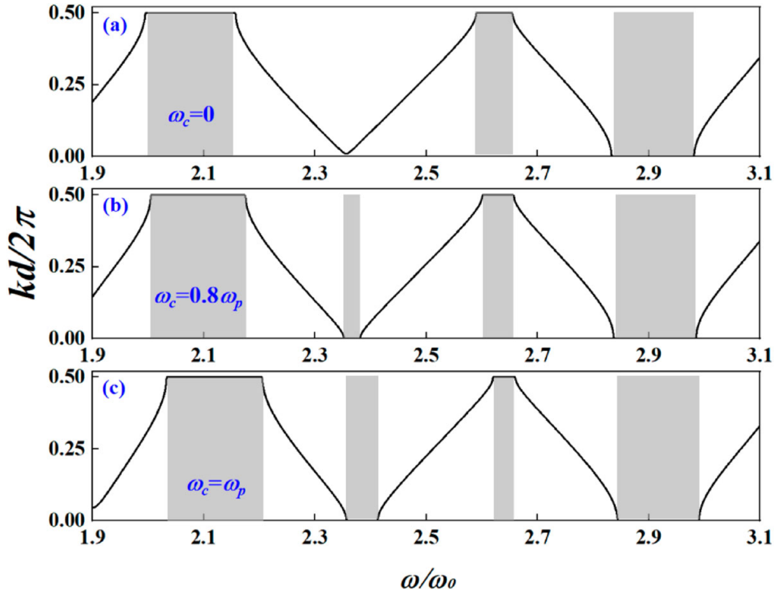

Figure 6. The influences of ω_c on dispersion relations if $r_0 = 20d$, $d_A = 0.2d$, $d_B = 0.35d$, $d_P = 0.45d$, $\omega_p = \omega_0$, $v_c = 0.0001\omega_p$, and $\alpha = 0$, (a) $\omega_c = 0$, (b) $\omega_c = 0.8\omega_p$, and (c) $\omega_c = \omega_p$.

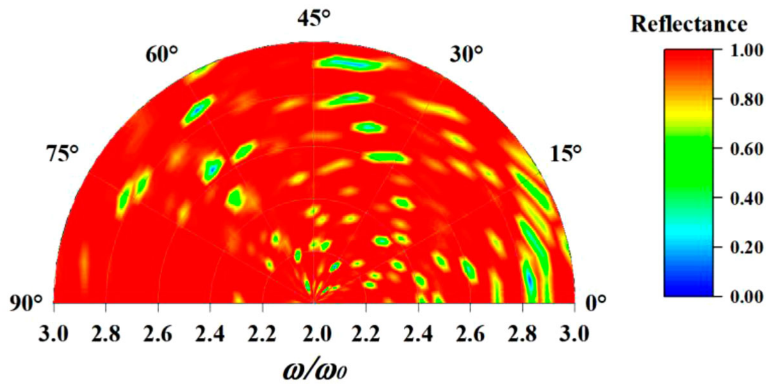

Figure 7. The reflection pattern under varying α with $r_0 = 20d$, $d_A = 0.2d$, $d_B = 0.35d$, $d_P = 0.45d$, $\omega_p = \omega_0$, $\omega_c = 0$, and $v_c = 0.0001\omega_p$.

by comparing the two. A comparison of Figures 13 and 14 reveals that the reflection spectra of the 1-D MPSPCs are extremely analogous to the 1-D PPCs, indicating that the 1-D MPSPCs have the same preeminent PBG properties as 1-D PPCs. However, unlike the 1-D PPCs, the 1-D MPSPCs also have absorption properties. While the absorption of the 1-D PPCs is extremely weak with identical structural parameters, the 1-D MPSPCs have conspicuous absorption properties, and they can be further optimized by adjusting the incidence angle and reducing the initial radius. Therefore, it is reasonable to speculate that 1-D MPSPCs not only have splendid PBG properties but also have absorption characteristics that 1-D PPCs do not possess, which are particularly consequential for applications.

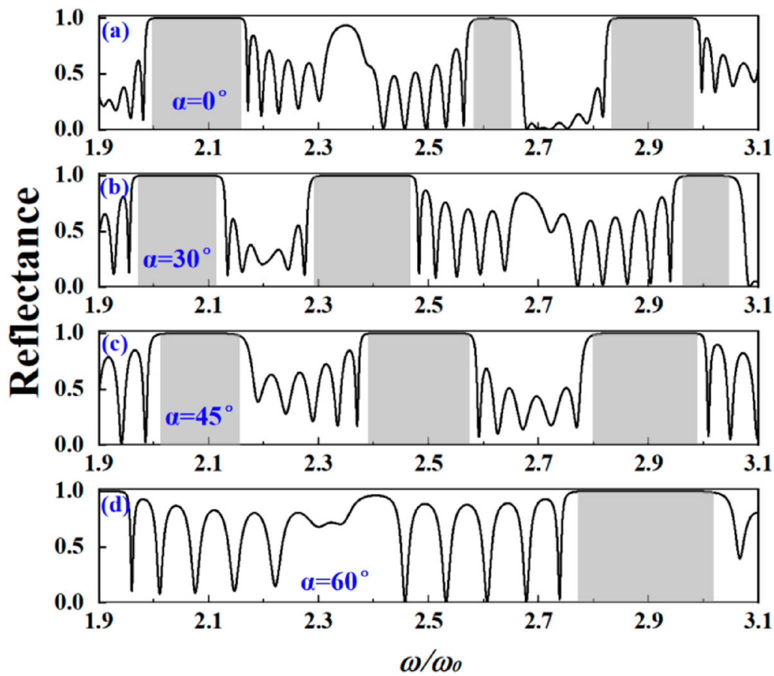

Figure 8. The reflection spectra in case of $r_0 = 20d$, $d_A = 0.2d$, $d_B = 0.35d$, $d_P = 0.45d$, $\omega_p = \omega_0$, $\omega_c = 0$, and $v_c = 0.0001\omega_p$ when (a) $\alpha = 0°$, (b) $\alpha = 30°$, (c) $\alpha = 45°$, and (d) $\alpha = 60°$.

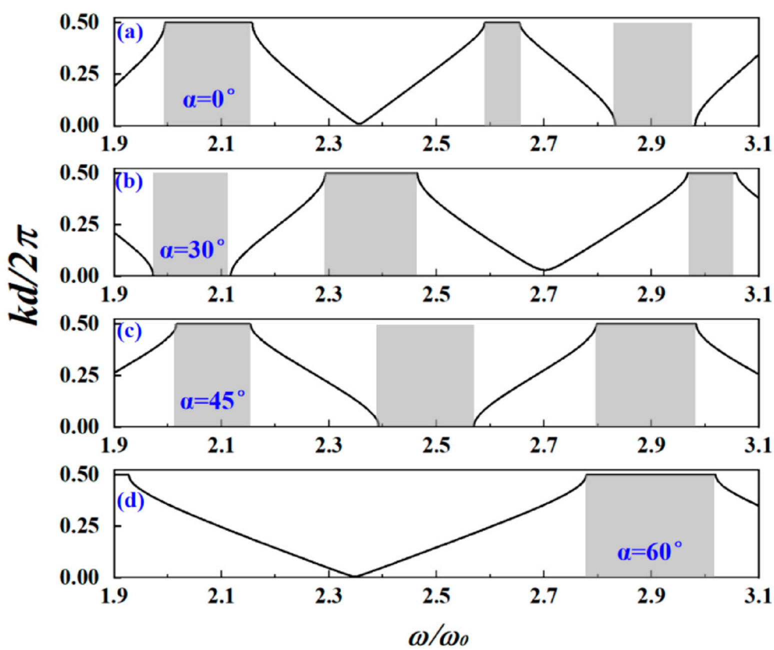

Figure 9. The dispersion relation curves with $r_0 = 20d$, $d_A = 0.2d$, $d_B = 0.35d$, $d_P = 0.45d$, $\omega_p = \omega_0$, $\omega_c = 0$, and $v_c = 0.0001\omega_p$ when (a) $\alpha = 0°$, (b) $\alpha = 30°$, (c) $\alpha = 45°$, and (d) $\alpha = 60°$.

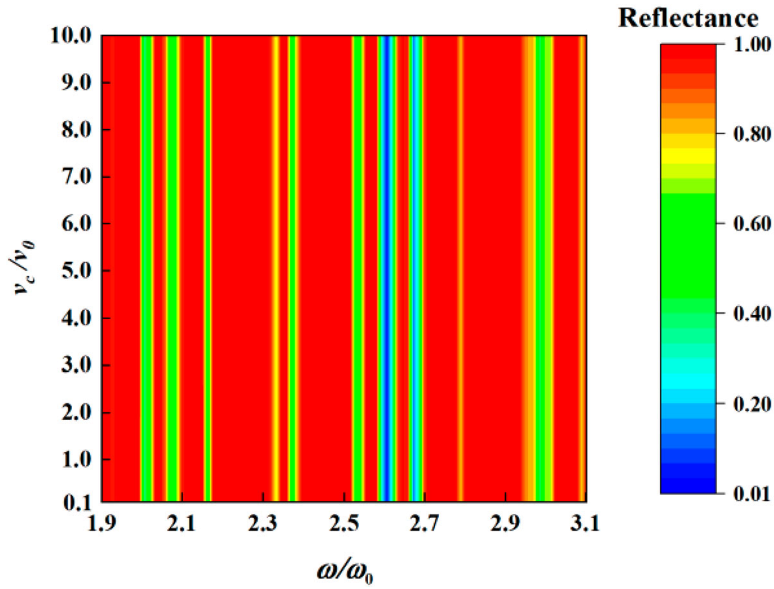

Figure 10. Change in reflection spectra of v_c rising from 0.1 to 10 defining $r_0 = 20d$, $d_A = 0.2d$, $d_B = 0.35d$, $d_P = 0.45d$, $\omega_p = \omega_0$, $\omega_c = 0$, and $\alpha = 0$ ($v_0 = 0.0001\omega_p$).

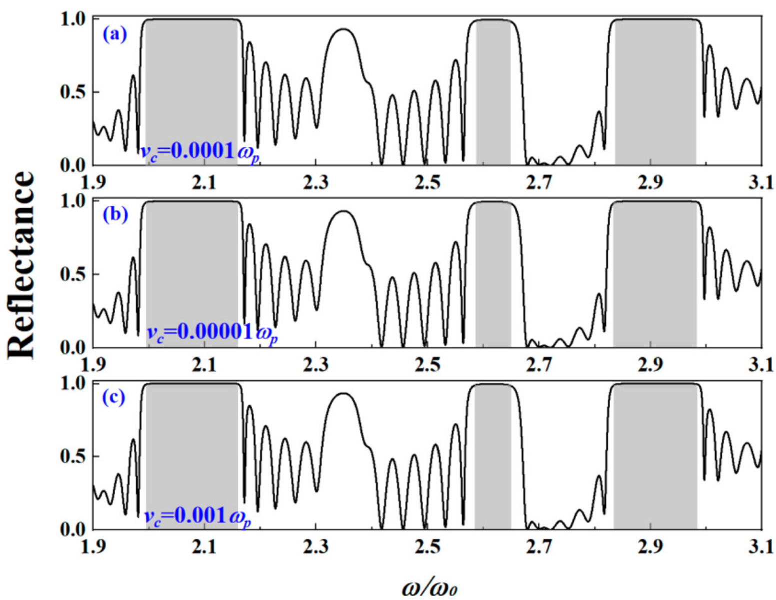

Figure 11. The chart regarding the influence of v_c on reflection spectra when $r_0 = 20d$, $d_A = 0.2d$, $d_B = 0.35d$, $d_P = 0.45d$, $\omega_p = \omega_0$, $\omega_c = 0$, and $\alpha = 0$, (a)$v_c = 0.0001\omega_p$, (b) $v_c = 0.00001\omega_p$, and (c) $v_c = 0.001\omega_p$.

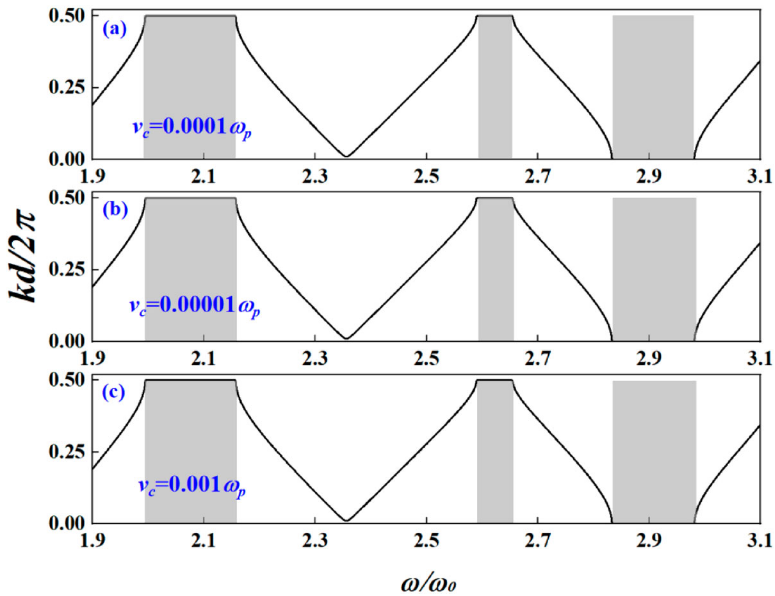

Figure 12. The chart regarding the influence of v_c on dispersion relation when $r_0 = 20d$, $d_A = 0.2d$, $d_B = 0.35d$, $d_P = 0.45d$, $\omega_p = \omega_0$, $\omega_c = 0$, and $\alpha = 0$, (a)$v_c = 0.0001\omega_p$, (b) $v_c = 0.00001\omega_p$, and (c) $v_c = 0.001\omega_p$.

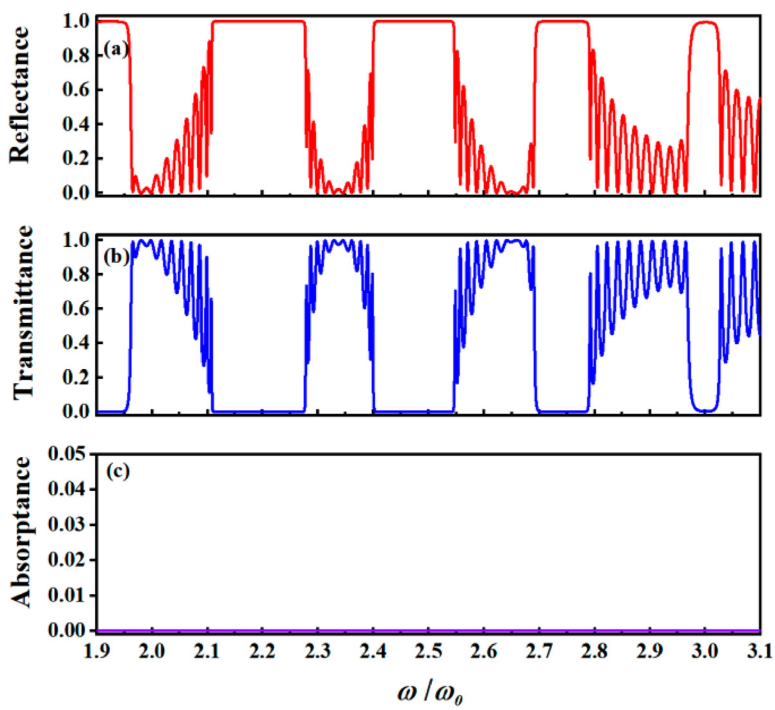

Figure 13. The reflection, transmission and absorption spectra of 1-D PPCs of TM waves with $r_0 = 20d$, $d_A = 0.2d$, $d_B = 0.35d$, $d_P = 0.45d$, $\omega_p = \omega_0$, $v_c = 0.0001\omega_p$, and $\alpha = 0$.

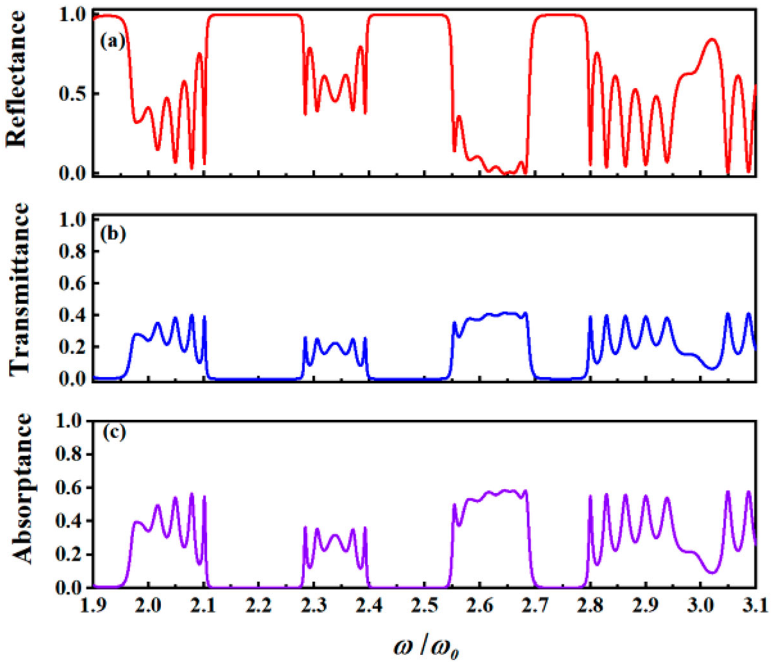

Figure 14. The reflection, transmission and absorption spectra of 1-D MPSPCs of TM waves in the case of $r_0 = 20d$, $d_A = 0.2d$, $d_B = 0.35d$, $d_P = 0.45d$, $\omega_p = \omega_0$, $v_c = 0.0001\omega_p$, and $\alpha = 0$.

By comparing Figures 14 and 15, we can easily find that the variations of the dissipation factor of dielectric K have no effect on the position and number of PBGs, and the two plots differ only in magnitude. In other words, the loss of energy only has an effect on the distribution of energy and has no bearing on the forbidden band peculiarities.

From Figure 16, the modification of ω_p has a considerable impact on the PBGs. The individual parameters are set as follows: $r_0 = 20d$, $d_A = 0.2d$, $d_B = 0.35d$, $d_P = 0.45d$, $v_c = 0.0001\omega_p$, $\omega_c = 0$, and $\alpha = 0$. When ω_p is less than $0.6\omega_0$, the tunability is pretty weak and the change of PBGs is extremely trifling. After ω_p enlarges to 0.6, the reflection spectrum is distinctly different from before, and the two-square marked areas in Figure 16 indicate the regions where the PBGs transform most dramatically, with alterations in the frequency range, bandwidth, and amount.

The reflection spectra and dispersion relationship curves of the proposed 1-D MPSPCs with ω_p are provided in Figures 17 and 18. The other parameters are configured as $r_0 = 20d$, $\omega_p = \omega_0$, $v_c = 0.0001\omega_p$, $\omega_c = 0$, and $\alpha = 0$. First of all, let $\omega_p = 0.6\omega_0$ and the PBGs can be expected at $\omega/\omega_0 = 1.97, 2.54$, and 2.81. The bandwidths of the PBGs are extraordinarily well-proportioned and the maximum bandwidth is $0.14\omega_0$. Following the line of variables discussion, increasing ω_p to $0.8\omega_0$, the positions of the PBGs shifted slightly, varying to be at $1.98\omega_0$, $2.56\omega_0$, and $2.82\omega_0$, and the frequency scale expanded marginally. Continuing to increase ω_p to ω_0, it is evidenced that PBGs show a comparable trend. It is worth mentioning that the number of PBGs aggrandizes for $\omega_p = 1.2\omega_0$, with PBGs at $2.01\omega_0$, $2.36\omega_0$, $2.63\omega_0$, and $2.85\omega_0$. The PBGs located at $2.01\omega_0$ and $2.85\omega_0$ do not change voluminously in terms of bandwidths, but the sharp decline in the bandwidth at $2.63\omega_0$ is presumed to be

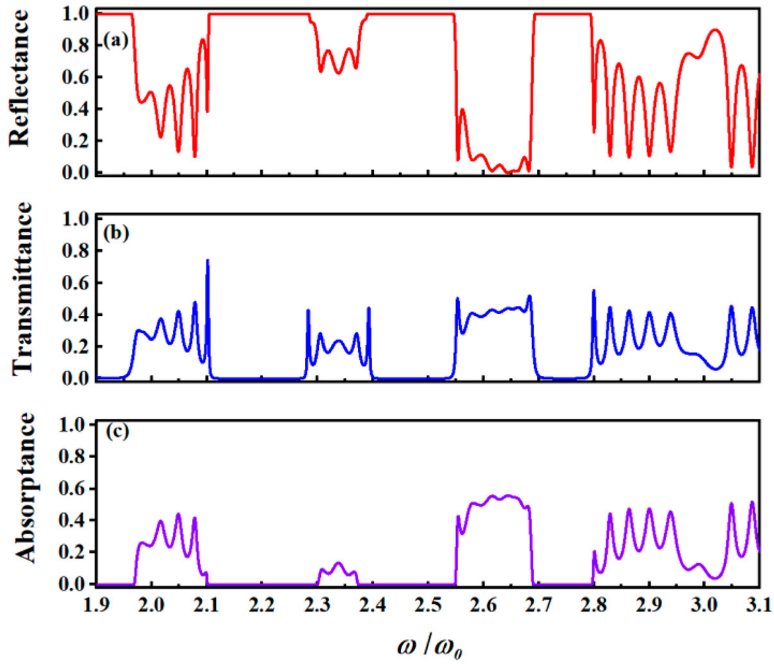

Figure 15. The reflection, transmission and absorption spectra of 1-D MPSPCs of TM waves with $r_0 = 20d$, $d_A = 0.2d$, $d_B = 0.35d$, $d_P = 0.45d$, $\omega_p = \omega_0$, $v_c = 0.0001\omega_p$, dissipation factor of dielectric K $\tan\sigma_e = 0.001$, and $\alpha = 0$.

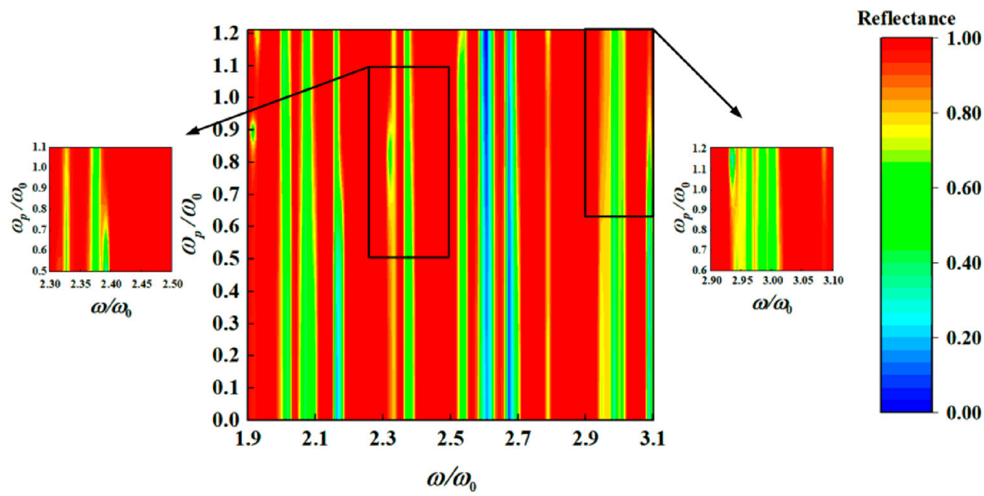

Figure 16. The graph of reflection with altering ω_p defining $r_0 = 20d$, $d_A = 0.2d$, $d_B = 0.35d$, $d_P = 0.45d$, $\omega_c = 0$, $v_c = 0.0001\omega_p$ and $\alpha = 0$.

caused by the formation of a new PBG at $2.36\omega_0$. ω_p is closely correlated with the electron density in the plasma layer, and an enlargement in the electron density leads to a rise in the energy consumption of the electromagnetic waves and thus to a phanerous variation

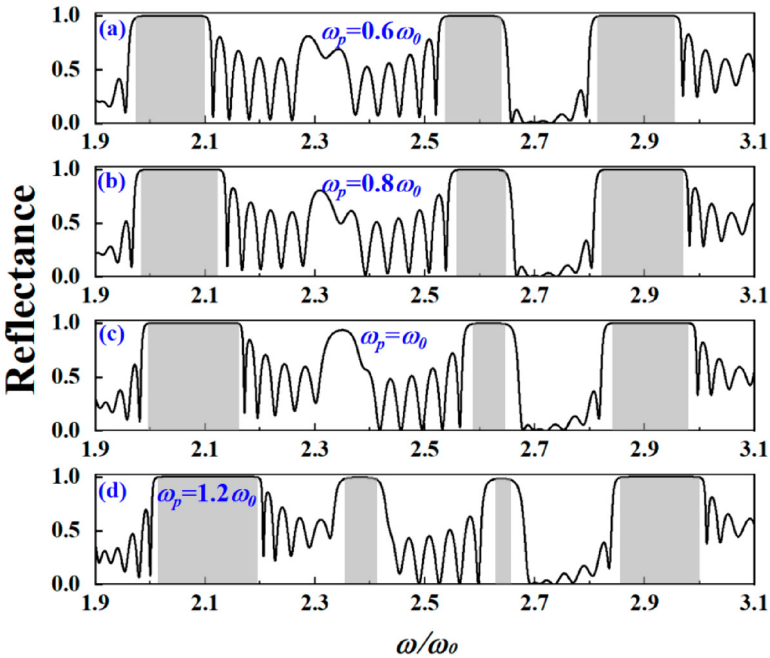

Figure 17. The reflection spectra about the influence of ω_p with $r_0 = 20d$, $d_A = 0.2d$, $d_B = 0.35d$, $d_P = 0.45d$, $\omega_c = 0$, $v_c = 0.0001\omega_p$, and $\alpha = 0$, (a) $\omega_p = 0.6\ \omega_0$, (b) $\omega_p = 0.8\omega_0$, (c) $\omega_p = \omega_0$, and (d) $\omega_p = 1.2\omega_0$.

in the transmission properties. It is necessary to complement that for the convenience of mathematical calculations, the Drude model is adopted with respect to the plasma [41]. The plasma frequency, as one of the crucial parameters of the plasma, is intimately intertwined with both density and temperature and is capable of reflecting the effects of density and temperature on 1-D MFSPCs transmission properties. Therefore, the temperature is not discussed separately here.

The medium thickness is a momentous factor affecting the PBGs. Also increasing the plasma thickness d_p, it can be seen in Figures 19(b) and 20(b) that PBGs are distributed at $\omega/\omega_0 = 1.95$, 2.21, and 2.50. In contrast, only two PBGs occur in the frequency range of $1.9\omega_0$–$3.1\omega_0$, located at $\omega/\omega_0 = 2.08$ and 2.73 as shown in Figures 19(c) and 20(c). The diminution of d_p also has an effect on the number of PBGs, with $d_A = 0.2d$, $d_B = 0.45d$, and $d_P = 0.35d$, a total of four PBGs are observed at $1.91\omega_0$, $2.12\omega_0$, $2.40\omega_0$, and $2.70\omega_0$, but the bandwidths of PBGs in this state are narrow. All things considered, the change in d_p has an enormous effect on PBGs and has prodigious control over their overall composition and frequency range. 1-D MPSPCs are sensitive to the adjustment of d_p by virtue of their geometrical properties. The high arbitrariness and adjustability of the PBGs distribution position are estimable for device design.

4. Conclusion

Generally speaking, this paper presents the first theoretical derivation of the transmission properties of 1-D MPSPCs. Employing TMM, the expressions for the transmittance,

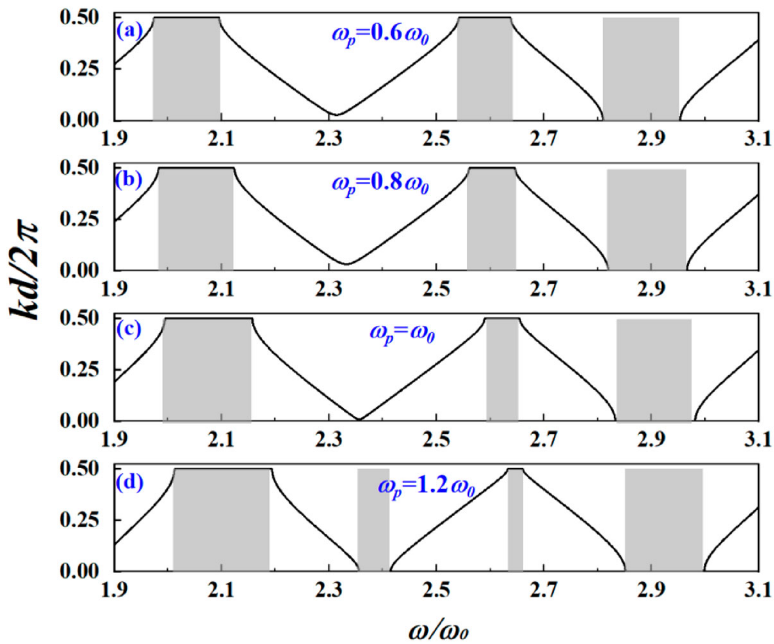

Figure 18. The dispersion relationship curves about the effects of $\omega_p$setting $r_0 = 20d$, $d_A = 0.2d$, $d_B = 0.35d$, $d_P = 0.45d$, $\omega_c = 0$, $v_c = 0.0001\omega_p$, and $\alpha = 0$, (a) $\omega_p = 0.6\omega_0$, (b) $\omega_p = 0.8\omega_0$, (c) $\omega_p = \omega_0$, and (d) $\omega_p = 1.2\omega_0$.

reflectance, and dispersion relations of 1-D MPSPCs under the TM waves are elicited. Meanwhile, the PBGs of 1-D MPSPCs are carefully analyzed by plotting the transmission spectra, reflection spectra, absorption spectra and dispersion relations curves. The reflection spectra of 1-D MPSPCs are in high agreement with the dispersion relation curves, which further proves the correctness of the theoretical derivation. The variables affecting 1-D MPSPCs are investigated in conjunction with the structure of the theoretical treatment. The effects of ω_c, α, v_c, ω_p, structure, tanσ_{e}, and d_p on the spectra and dispersion relation curves are analyzed, respectively. By varying the values of the variables, it turns out that the impact of v_c on the PBGs is extremely tiny. There is a correlation between ω_p and ω_c, and the influences on PBGs are quite akin, prevailingly in making the position of PBGs move toward high frequencies and accompanied by the expansion of PBGs bandwidth and the enhancement in the number of them. The alterations of the α and medium thickness will not only affect the position of PBGs but also the number of PBGs. Increasing both the incidence angle and plasma thickness can reduce the number and increase the bandwidth of PBGs. Structure and tanσ_{e} have implications for energy distribution but no control on PBGs. And the reduction of plasma thickness can result in an increment in the number of PBGs. The properties of 1-D MPSPCs are similar to that of 1-D PPCs, but 1-D MPSPCs are more sensitive to the change of variables and have momentous practical significance in tunable devices and curved reflectors.

Disclosure statement

No potential conflict of interest was reported by the author(s).

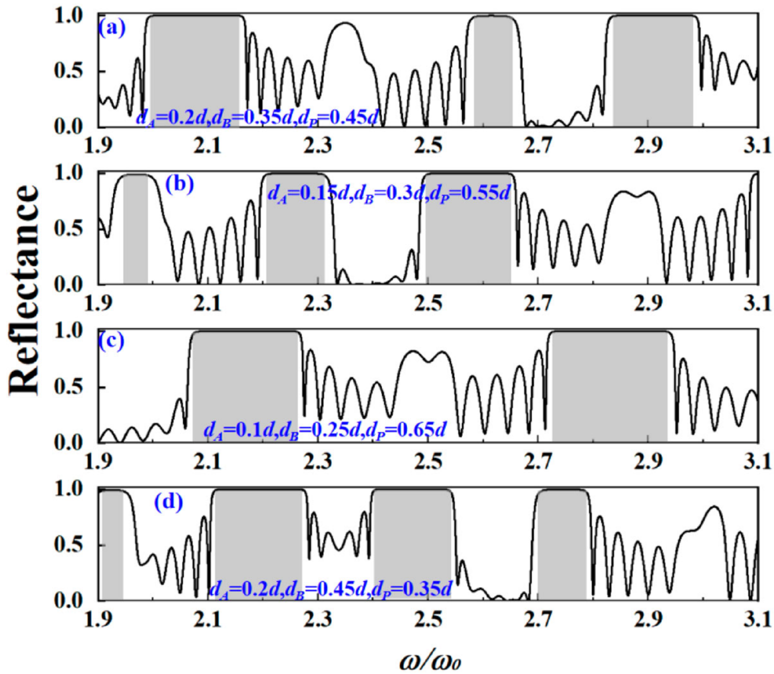

Figure 19. The picture concerning the influence of d_p on reflection spectra at $r_0 = 20d$, $\omega_p = \omega_0$, $v_c = 0.0001\omega_p$, $\omega_c = 0$, and $\alpha = 0$, (a)$d_A = 0.2d$, $d_B = 0.35d$, $d_P = 0.45d$, (b) $d_A = 0.15d$, $d_B = 0.3d$, $d_P = 0.55d$, (c) $d_A = 0.1d$, $d_B = 0.25d$, $d_P = 0.65d$, and (d) $d_A = 0.2d$, $d_B = 0.45d$, $d_P = 0.35d$.

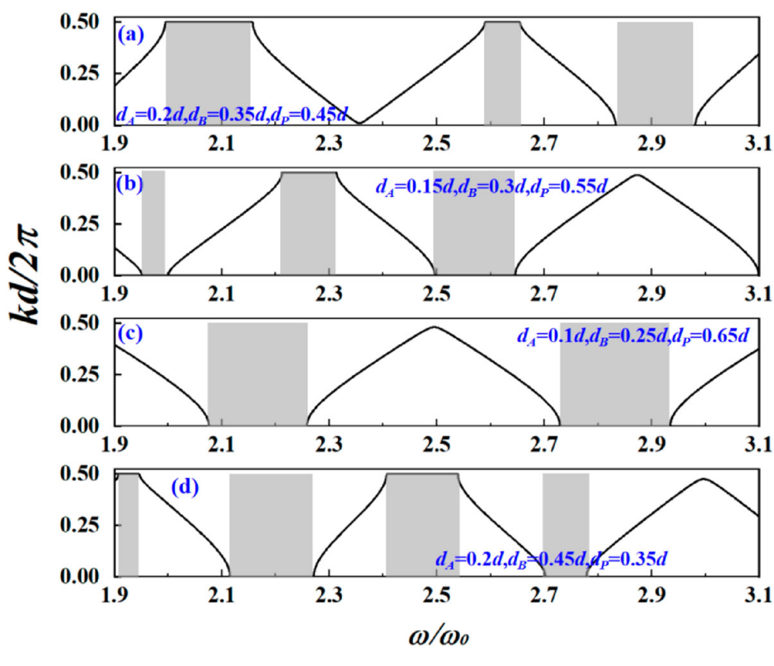

Figure 20. The picture concerning the effects of d_p on dispersion relations if $r_0 = 20d$, $\omega_p = \omega_0$, $v_c = 0.0001\omega_p$, $\omega_c = 0$, and $\alpha = 0$, (a)$d_A = 0.2d$, $d_B = 0.35d$, and $d_P = 0.45d$, (b) $d_A = 0.15d$, $d_B = 0.3d$, and $d_P = 0.55d$, (c) $d_A = 0.1d$, $d_B = 0.25d$, and $d_P = 0.65d$, and (d) $d_A = 0.2d$, $d_B = 0.45d$, $d_P = 0.35d$.

Funding

This work was supported by the College Student Innovation Training Program of Nanjing University of Posts and Telecommunications.

References

[1] Yablonovitch E. Inhibited spontaneous emission in solid-state physics and electronics. Phys Rev Lett 1987;58(20):2059–2062.
[2] John S. Strong localization of photons in certain disordered dielectric superlattices. Phys Rev Lett 1987;58(23):2486–2489.
[3] Joannopoulos JD, Villeneuve PR, Fan S. Photonic crystals: putting a new twist on light. Nature. 1997;386:143–149.
[4] Leung KM, Liu YF. Full vector wave calculation of photonic band structures in face-centered-cubic dielectric media. Phys Rev Lett 1990;65(21):2646.
[5] Li ZY, Lin LL, Zhang ZQ. Spontaneous emission from photonic crystals: full vectorial calculations. Phys Rev Lett 2000;84(19):4341–4344.
[6] Hong BB, Feng N, Chen J, et al. Substrate integrated Bragg waveguide: an octave-bandwidth single-mode hybrid transmission line for millimeter-wave applications. Opt Express. 2020;28(19):27903–27918.
[7] Li HS, Low MX, Ako R, et al. Broadband single-mode hybrid photonic crystal waveguides for terahertz integration on a chip. Adv Mater Technol. 2020;5(7):2000117.
[8] Zaky ZA, Ahmed AM, Shalaby AS, et al. Refractive index gas sensor based on the Tamm state in a one-dimensional photonic crystal: theoretical optimization. Sci Rep. 2020;10(1):9736.
[9] Matniyaz T, Bingham SP, Kalichevsky-Dong MT, et al. High-power single-frequency single-mode all-solid photonic bandgap fiber laser with kHz linewidth. Opt Lett. 2022;47(2):377–380.
[10] Benjamin P, Holten R, Matniyaz T, et al. kW-level monolithic single-mode narrow-linewidth all-solid photonic bandgap fiber amplifier. Opt Lett. 2021;46(18):4458–4461.
[11] Aly AH, Mohamed D, Mohaseb MA. Metamaterial control of hybrid multifunctional high-Tc superconducting photonic crystals for 1D quasi-periodic structure potential applications. Mater. Res.. 2020;23(3):0695.
[12] Aly AH, Mohamed D. The optical properties of metamaterial-superconductor photonic band gap with/without defect layer. J Supercond Novel Magn. 2019;32:1897–1902.
[13] Aly AH, Sabra W, Elsayed HA. Cutoff frequency in metamaterials photonic crystals within terahertz frequencies. Int J Mod Phys B. 2017;31:1750123.
[14] Aly AH, Ryu S-W, Hsu H-T, et al. THz transmittance in one-dimensional superconducting nanomaterial-dielectric superlattice. Mater Chem Phys. 2009;113:382–384.
[15] Aly AH, Abdel Ghany SE-S, Kamal BM, et al. Theoretical studies of hybrid multifunctional $YaBa_2Cu_3O_7$ photonic crystals within visible and infra-red regions. Ceram Int. 2020;46:365–369.
[16] Awad MA, Aly AH. Experimental and theoretical studies of hybrid multifunctional TiO_2/TiN/TiO_2. Ceram Int. 2019;45:19036–19043.
[17] Aly AH, Mohamed D. Bscco/$SrTiO_3$ One dimensional superconducting photonic crystal for many applications. J Supercond Novel Magn. 2015;28:1699–1703.
[18] Aly AH, Ameen AA, Mahmoud MA, et al. Photonic crystal enhanced by metamaterial for measuring electric permittivity in GHz range. Photonics. 2021;8:416.
[19] Natesan A, Govindasamy KP, Gopal TR, et al. Tricore photonic crystal fibre based refractive index sensor for glucose detection. IET Optoelectron. 2019;13(3):118–123.
[20] Aly AH, Awasthi SK, Mohaseb MA, et al. Matlab simulation-based theoretical study for detection of a wide range of pathogens using 1D defective photonic structure. Crystals (Basel). 2022;12:220.
[21] Aly AH, Awasthi SK, Mohamed AM, et al. 1D reconfigurable bistable photonic device composed of phase change material for detection of reproductive female hormones. Phys Scr. 2021;96:125533.

[22] Amiri IS, Paul BK, Ahmed K, et al. Tri-core photonic crystal fiber based refractive index dual sensor for salinity and temperature detection. Microw Opt Technol Lett. 2019;61:847–852.
[23] Zaky ZA, Panda A, Pukhrambam PD, et al. The impact of magnetized cold plasma and its various properties in sensing applications. Sci Rep. 2022;12:3754.
[24] Aly AH, Ameen AA, Mahmoud MA, et al. Photonic crystal enhanced by metamaterial for measuring electric permittivity in GHz range. Photonics. 2021;8:416.
[25] El-Naggar SA. Properties of defect modes in cylindrical photonic crystals. Optik (Stuttg). 2020;200(C):163447–163447.
[26] Fernandes JA, Anselmo DHAL, Vasconcelos MS, et al. A study of transmission on cylindrical photonic quasicrystals. Opt Mater (Amst). 2021;121:111566.
[27] Hu CA, Wu CJ, Yang TJ, et al. Analysis of optical properties in cylindrical dielectric photonic crystal. Opt Commun. 2013;291:424–434.
[28] Jiang Y, Hacker J. Cylindrical-wave reflection and antireflection at media interfaces. Appl Opt. 1994;33(31):7431–7434.
[29] Jiang Y, Hacker J. Distributed-Bragg reflectors and 90° couplers for cylindrical wave devices. Appl Phys Lett. 1993;63(11):1453–1455.
[30] El-Naggar SA. Optical guidance in cylindrical photonic crystals. Optik (Stuttg). 2017;130:584–588.
[31] Larsen T, Bjarklev A, Hermann D, et al. Optical devices based on liquid crystal photonic bandgap fibres. Opt Express. 2003;11(20):2589–2596.
[32] Jeong K. Study on electromagnetic wave propagation characteristics in cylindrical photonic crystal waveguides with high-index cores. Int J Energy Inf Commun. 2019;10(2):1–6.
[33] Laviada J, Pino MR, Las-Heras F. Characteristic spherical wave expansion with application to scattering and radiation problems. IEEE Antennas Wirel Propag Lett. 2009;8:599–602.
[34] Moreira WL, Neves AAR, Garbos MK, et al. Expansion of arbitrary electromagnetic fields in terms of vector spherical wave functions. Opt Express. 2016;24(3):2370–2382.
[35] Wang Z, Zhang X, Lv GQ, et al. Hybrid holographic Maxwellian near-eye display based on spherical wave and plane wave reconstruction for augmented reality display. Opt Express. 2021;29(4):4927–4935.
[36] Xu BG, Zhang DG, Wang Y, et al. Characterization of millimeter wave photonic crystal circulator with a ferrite sphere. Results Phys. 2022;34:105315.
[37] Li L, Li J, Meng T, et al. Diethylamine fluorescence sensor based on silica hollow sphere photonic crystals. Anal Methods. 2021;13:2189–2195.
[38] Hojo H, Mase A. Dispersion relation of electromagnetic waves in one-dimensional plasma photonic crystals. J Plasma Fusion Res. 2004;80(2):89–90.
[39] Shiveshwari L, Mahto P. Photonic band gap effect in one-dimensional plasma dielectric photonic crystals. Solid State Commun. 2006;138(3):160–164.
[40] Liu S, Zhong SY, Liu SQ. A study of properties of the photonic band gap of unmagnetized plasma photonic crystal. Plasma Sci Technol. 2009;11(1):14–17.
[41] Qi LM, Yang ZQ, Lan F, et al. Properties of obliquely incident electromagnetic wave in one-dimensional magnetized plasma photonic crystals. Phys Plasmas. 2010;17(4):042501.
[42] Liang YC, Liu Z, Peng J, et al. Study on transmission characteristics and bandgap types of plasma photonic crystal. Photonics. 2021;8(9):401–401.
[43] Wan BF, Wang P-X, Xu Y, et al. A space filter possessing polarization separation characteristics realized by 1-D magnetized plasma photonic crystals. IEEE Trans Plasma Sci. 2021;49(2):703–710.
[44] Ma Y, Zhang T, Mao MY, et al. A switchable absorption-transmission window modulator based on 1-D magnetized plasma photonic crystals. IEEE Trans Plasma Sci. 2020;48(12):4155–4162.
[45] Xu MC, Liu S, Zhong SY. The properties of a tunable terahertz multichannel filter from one-dimensional photonic crystal dope by magnetized plasma defect. Opt Quantum Electron. 2019;51(4):1–11.
[46] Wang QY, Wang PX, Wan BF, et al. Investigation on the nonreciprocal properties of one-dimensional cylindrical magnetized plasma photonic crystals. J Opt Soc Am A. 2021;38(6):897–907.
[47] Moreira WL, Neves AAR, Garbos MK, et al. Expansion of arbitrary electromagnetic fields in terms of vector spherical wave functions. Opt Express. 2016;24:2370–2382.

[48] Zhang J, Meng Z, Liu J, et al. Spherical colloidal photonic crystals with selected lattice plane exposure and enhanced color saturation for dynamic optical displays. ACS Appl Mater Interfaces. 2019;11:42629–42634.
[49] Xu BG, Zhang DG, Wang Y, et al. Characterization of millimeter wave photonic crystal circulator with a ferrite sphere. Results Phys. 2022;34:105315.
[50] Wang K, Li C, Li Z, et al. A facile fabrication strategy for anisotropic photonic crystals using deformable spherical nanoparticles. Nanoscale. 2019;11:14147–14154.